Materials Horizons

ROYAL SOCIETY OF CHEMISTRY

COMMUNICATION

View Article Online
View Journal

Cite this: DOI: 10.1039/d5mh02224j

Received 22nd November 2025,
Accepted 10th February 2026

DOI: 10.1039/d5mh02224j

rsc.li/materials-horizons

Gate-controlled neuromodulatory optical synaptic transistor for adaptive learning and energy-accuracy balance

Jung Min Yun, Yu Bin Kim, Min Jung Choi and Seong Jun Kang *

Neuromorphic vision systems demand highly efficient optical signal acquisition and adaptable, energy-aware learning capabilities. Optical synaptic transistors have emerged as promising components for in-sensor computing by directly responding to visual stimuli and mimicking core synaptic functions such as excitatory postsynaptic current (EPSC), paired-pulse facilitation (PPF), and both short- and long-term plasticity. However, most devices demonstrate fixed synaptic gain, limiting their ability to adapt learning behavior in response to varying input conditions or computational tasks. Inspired by biological neuromodulation, we present a gate-tunable optical synaptic transistor based on an In–Ga–Zn–O (IGZO) phototransistor that supports both conventional synaptic behaviors and voltage-dependent modulation of learning sensitivity. The device allows pre-conditioning of EPSC amplitude *via* gate bias prior to optical stimulation, effectively mimicking neuromodulatory gain control. Convolutional Neural Network (CNN) training on the CIFAR-10 dataset shows that higher gate biases improve classification accuracy with higher energy use, while weaker biases reduce energy consumption with an adaptive accuracy tradeoff. Our device integrates core synaptic behaviors with gate-controlled gain modulation, effectively emulating neuromodulation and offering a practical and efficient approach to adaptive neuromorphic vision systems.

New concepts

This work presents an oxide-based optical synaptic transistor that emulates biological neuromodulation by enabling pre-adjustment of synaptic gain *via* gate voltage before light stimulation. In biology, neuromodulators such as dopamine regulate synaptic strength, sensitivity, and learning rate without directly triggering activity. Gate-controlled carrier modulation combined with intrinsic oxygen-vacancy traps in IGZO enables tunable optical plasticity and supports both short- and long-term synaptic functions. The intrinsic oxygen-vacancy trap states extend the photoresponse into the visible range and induce persistent photoconductivity, providing the physical basis for adjustable optical gain. Identical optical stimuli yield different synaptic responses depending on the preset gate bias, allowing flexible control of learning behavior. When applied to a convolutional neural network (CNN), higher gate-induced EPSC improved classification accuracy, while lower bias reduced energy consumption. This work demonstrates visible-light-driven synaptic modulation that mimics neuromodulator function using gate control in a single oxide-based optical synaptic device.

1. Introduction

The human brain has an extraordinary ability to process and learn from large amounts of sensory information in real time with exceptional energy efficiency. This ability is mainly due to the highly parallel and distributed structure of biological neural networks, where learning and memory take place locally at synaptic junctions through experience-driven synaptic plasticity. Among the different sensory modalities, vision-based learning is particularly important, as it supports a wide range of human cognitive and behavioral functions. As a result, replicating synaptic behavior at the hardware level, especially for visual information processing, has become a key focus in neuromorphic electronics.[1–6]

To emulate brain like visual learning, optoelectronic synaptic devices have attracted considerable attention.[7,8] These devices combine light sensing and memory functions in a single platform, enabling direct processing of optical signals at the sensor level. This ''in-sensor computing'' approach removes the need for separate image sensing and processing units, improving speed and reducing energy use.[7,9–15] However, despite notable progress, most reported optical synaptic transistors display fixed synaptic gain properties, meaning the strength of the excitatory postsynaptic current (EPSC) is determined only by the intensity or duration of the optical input.[16] This limits their adaptability and learning flexibility, especially in systems that require variable learning speeds or stimulus sensitivity.[17,18]

In contrast, biological synapses show more adaptable and context-sensitive learning behavior through the effects of

Department of Materials Science and Engineering, Kyung Hee University, Yongin 17104, Republic of Korea. E-mail: junkang@khu.ac.kr; Tel: +82-31-201-3324

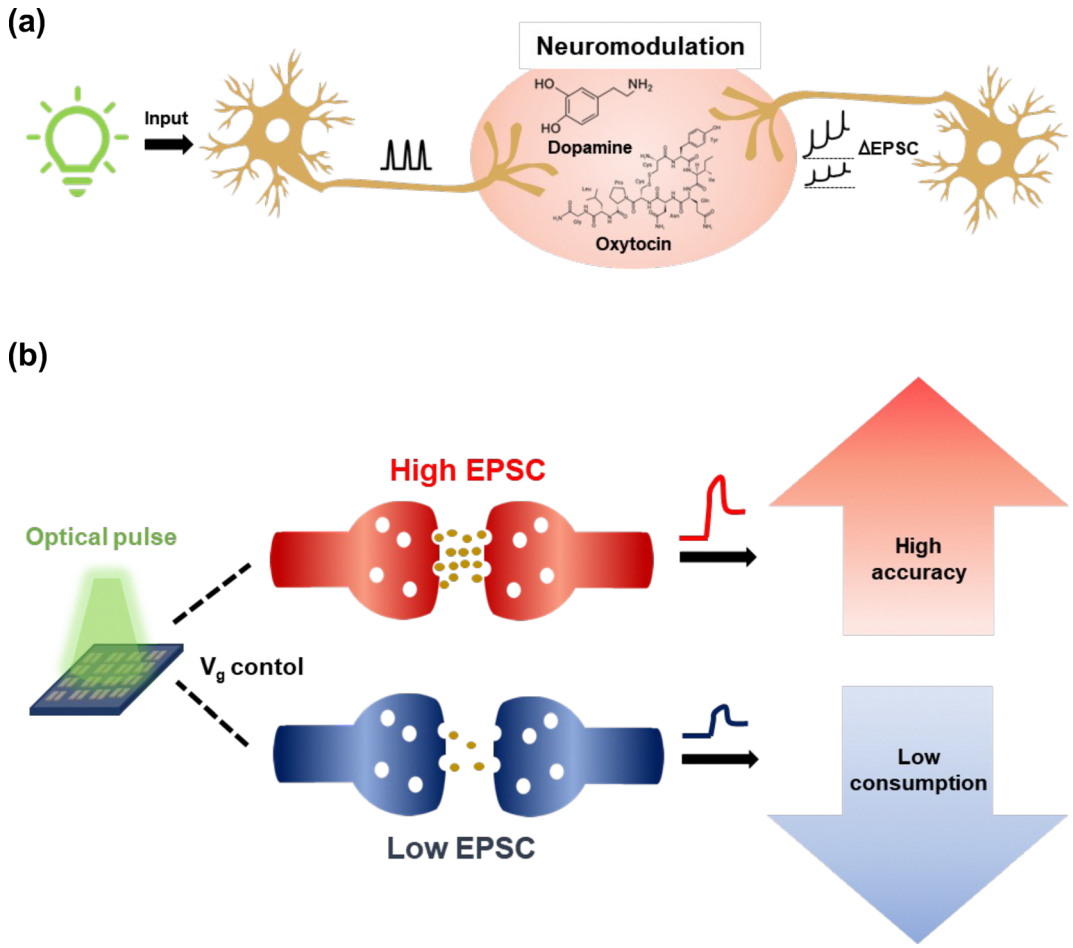

Fig. 1 (a) Schematic illustration of neuromodulation in a biological synapse. (b) Gate-tunable optical synaptic transistor mimicking biological neuromodulation. Under identical optical stimuli, different gate voltages induce varying excitatory postsynaptic current (EPSC) levels.

neuromodulators such as dopamine, acetylcholine, and oxytocin. These molecules do not directly trigger postsynaptic responses but instead regulate the sensitivity and plasticity of synapses either before or during stimulation.[19–21] For example, dopamine release can lower the threshold for long-term potentiation (LTP), resulting in greater synaptic weight change in response to the same input. This process, known as neuromodulation, enables context dependent learning, where identical stimuli can produce different learning outcomes depending on the neuromodulatory state of the network.[17,22–24] As illustrated in Fig. 1a, such neuromodulators play critical roles in adjusting synaptic gain in accordance with internal or external context.

In the context of neuromorphic computing, this concept can be directly mapped onto our device framework. Optical excitation in the IGZO channel increases carrier density, leading to an excitatory postsynaptic current (EPSC) that functions as the synaptic weight in a neural network. In this analogy, the gate voltage plays a role similar to biological neuromodulators such as dopamine or oxytocin, regulating the degree of carrier accumulation and thereby modulating the effective synaptic gain. As illustrated in Fig. 1b, the gate bias acts as an external modulatory input that tunes the channel state, analogous to how neuromodulators modulate synaptic efficacy in biological systems. Consequently, the amplitude of the EPSC determines the learning strength or weight update in the CNN, establishing a clear correspondence between material-level charge dynamics and algorithm-level learning behavior.

Inspired by this mechanism, we present a gate-tunable optical synaptic transistor enabling pre-adjustment of the postsynaptic response before optical stimulation. Our device uses an indium gallium zinc oxide (IGZO) channel in a phototransistor configuration, in which gate voltages modulate the carrier distribution and synaptic strength. Under the same optical input, the device produces distinct EPSC values depending on the gate bias. The device is sensitive to both blue and green light, enabling synaptic behavior under visible-light excitation. This spectral sensitivity ensures compatibility with practical light sources and supports wavelength-selective, energy-efficient neuromorphic vision operation.[25,26] This pre-conditioning enables tunable learning rates, controllable energy–accuracy balance, and flexible synaptic response modulation. To examine its functional impact, we trained a convolutional neural network (CNN) using the CIFAR-10 dataset under different gate voltage conditions.[27] Using experimentally measured EPSCs as synaptic weights, stronger gate biases improve learning accuracy, though at the cost of increased energy consumption. Lower gate biases reduce

accuracy but enhance energy efficiency, showcasing a biologically inspired tradeoff.[28,29] These findings highlight the potential of gate-tunable optical synaptic transistors for enabling adaptive, low-power neuromorphic vision hardware that closely mirrors human learning processes.[30]

2. Experimental section

2.1. Materials

A 0.1 M IGZO precursor solution was prepared by dissolving indium nitrate hydrate ($In(NO_3)_3{\cdot}xH_2O$, Thermo Fisher Scientific), gallium nitrate hydrate ($Ga(NO_3)_3{\cdot}xH_2O$, Sigma-Aldrich), and zinc nitrate hexahydrate ($Zn(NO_3)_2{\cdot}6H_2O$, Sigma-Aldrich) in 2-methoxyethanol (Daejung) with a molar ratio of 6 : 1 : 2. The mixed solution was stirred at 80 °C for 1 hour.[16]

2.2. Device fabrication

Bottom-gate, top-contact synaptic transistors were fabricated on SiO_2 (100 nm)/p++Si substrates. The substrates were sequentially cleaned in deionized (DI) water, acetone, and isopropyl alcohol (IPA) using an ultrasonicator, with each step lasting 15 minutes. To further remove organic residues and enhance surface hydrophilicity, a UV-ozone treatment (UVC-160, Omniscience) was applied for 15 minutes. The IGZO solution was spin-coated onto the substrate at 4000 rpm for 30 seconds, followed by thermal annealing at 350 °C in ambient air for 1 hour. Aluminum source and drain electrodes (100 nm thick) were deposited using thermal evaporation through a shadow mask. The resulting devices had a channel length and width of 100 μm and 1000 μm, respectively.

2.3. Characterization

2.3.1. Electrical and optical characterization. The electrical and synaptic characteristics of the fabricated IGZO-based optical neuromorphic transistors were measured using a semiconductor parameter analyzer (Keithley 2636A). For optical stimulation, a tunable light source (Thorlabs) was used to provide monochromatic illumination. The optical transmittance of the IGZO films was measured using a UV-vis spectrophotometer (Cary 100). X-ray photoelectron spectroscopy (XPS, Thermo Fisher Scientific) and Ultraviolet photoelectron spectroscopy (UPS, Scienta omicron) analyses were performed, using an Al Kα X-ray source (1486.6 eV) and a He I ultraviolet source (21.22 eV), respectively.

2.3.2. Machine learning simulation. All convolutional neural network (CNN) simulations were performed in the Google Colab (free tier) environment using Python 3.12.12 and TensorFlow 2.19.0 with the tf.keras API. NumPy 2.0.2 and pandas 2.2.2 were used for numerical computation and data handling, respectively.[32–34] Machine learning classification was performed using the CIFAR-10 dataset (10 classes, 32 × 32 RGB images). All images were normalized to [0, 1] and split into training (50 000 images) and test sets (10 000 images). EPSC values measured under different gate biases were normalized and assigned as synaptic weights in a convolutional neural network (CNN). To validate the impact of device-derived synaptic weights, three training scenarios were compared: a baseline model using standard Xavier initialization without device influence, an optimal device mode in which weights were scaled by the normalized EPSC obtained at V_G = −3 V, and a low-power mode using EPSC values at V_G = −18 V. The experimentally measured EPSC values were not directly assigned as CNN synaptic weights. Instead, the EPSC values obtained under different gate voltages were normalized and used as multiplicative scaling factors applied to the initial weights generated by standard Xavier initialization. Specifically, the initial weights were defined as:

$$W_{\text{init}}^{\text{EPSC}} = \alpha \cdot \frac{\text{EPSC}(V_G)}{\text{EPSC}_{\text{max}}} \cdot W_{\text{init}}^{\text{Xavier}}$$

where $W_{\text{init}}^{\text{EPSC}}$ represensts the EPSC-modulated initial weight tensor used to initialize the CNN prior to training, $W_{\text{init}}^{\text{Xavier}}$ denotes the conventionally initialized weights, EPSC(V_G) is the experimentally measured EPSC under a given gate voltage, EPSC_{max} corresponds to the maximum EPSC value measured across all gate voltages and illumination conditions used for normalization, and α is a scaling constant set to unity. This approach allows the device-derived EPSC to act as a neuromodulatory prior that biases the initial learning trajectory while preserving identical network architectures and backpropagation algorithms.

All models shared the same architecture (Conv2D: 32 → 64 → 128, Dense: 128 → 10) with tanh activation for all hidden layers, and were trained using stochastic gradient descent with a learning rate of 0.01 and a batch size of 32 for 20 epochs. The experimentally measured EPSC values under different gate voltages were normalized and applied as multiplicative scaling factors to the initial weights of all convolutional and fully connected layers prior to training. After this initialization step, all models were trained using identical backpropagation settings without further device involvement. This approach allows the device-derived EPSC to act as a neuromodulatory prior that biases the initial learning trajectory while preserving identical network architectures and training conditions.

2.3.3. Optoelectronic characteristics measurement. The optoelectronic response of the device was characterized using a semiconductor parameter analyzer (Keithley 2636A) connected to a probe station. Monochromatic light sources with wavelengths of 450 nm (blue) and 520 nm (green) were used as optical stimuli. The device was tested under both long (1 s interval) and short (25 ms interval) light pulse conditions to examine its temporal response characteristics. Furthermore, illumination intensities of 4.5, 3.2, and 1.6 mW cm^{-2} were applied to investigate the light intensity-dependent photocurrent and EPSC behaviors.

3. Results and discussion

Fig. 2 shows the synaptic functions and gate voltage-dependent modulation characteristics of the proposed IGZO-based optical synaptic transistor. As illustrated in Fig. 2a, the device uses a phototransistor structure with an IGZO channel on a SiO_2/Si substrate and an Al top electrode. When optical pulses hit the channel vertically, photocarriers are generated and trigger synaptic responses. The transfer curves in Fig. 2b show that

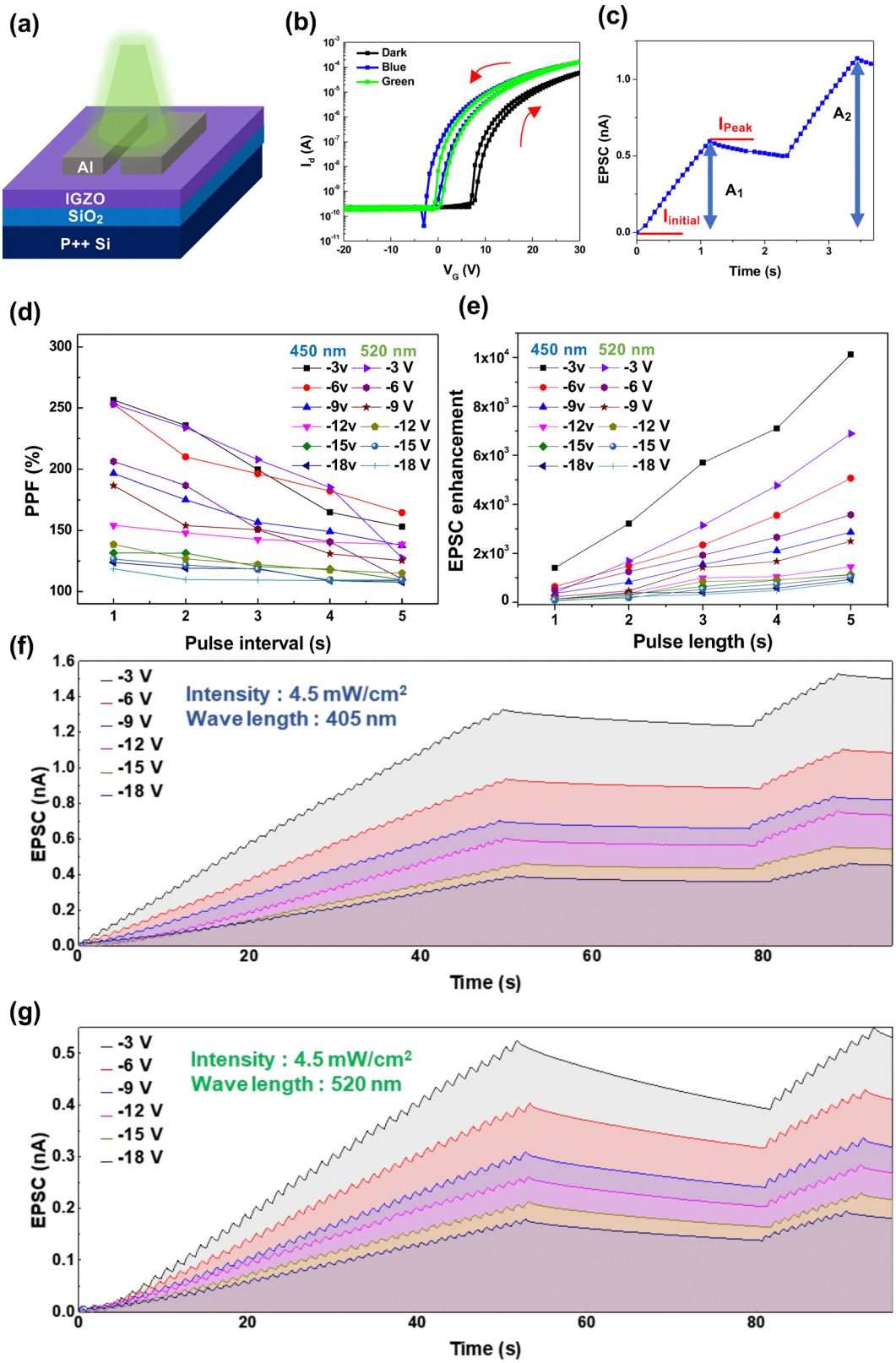

Fig. 2 (a) Schematic structure of the IGZO-based optical synaptic transistor, consisting of a phototransistor configuration with an IGZO channel and Al top electrodes (b) transfer curves under dark, 450 nm (blue), and 520 nm (green) illumination, showing photoresponsive characteristics in the visible range (c) typical excitatory postsynaptic current (EPSC) response to two consecutive light pulses, demonstrating paired-pulse facilitation (PPF) (d) PPF (%) extracted at various pulse intervals under under 12 conditions (6 gate voltages × 2 wavelengths) (e) EPSC enhancement as a function of optical pulse duration under 12 conditions (6 gate voltages × 2 wavelengths) (f and g) Learning–forgetting–relearning experiments under 450 nm (f) and 520 nm (g) light: 50 cycles of optical pulses (learning), 50 s (forgetting), and 10 additional pulses (relearning).

the device responds strongly to both 405 nm (blue) and 520 nm (green) light compared to the dark state. The negative shift in threshold voltage under illumination is attributed to photoexcited electrons generated from oxygen-vacancy-related trap states in the IGZO channel. These photocarriers accumulate near the IGZO/SiO_2 interface, reducing the gate bias required for channel conduction. In addition, some electrons become trapped in oxygen-vacancy sites, leading to a persistent photoconductivity effect and a slight increase in hysteresis during dual-direction gate sweeps. This confirms that the device operates effectively in the visible light range, making it both energy-efficient and suitable for practical optical neuromorphic systems.[35–37] To investigate short-term synaptic behavior, we measured paired-pulse facilitation (PPF). Fig. 2c displays a typical EPSC response to two consecutive light pulses.[38,39] The synaptic transmission behavior of the device can be understood by analogy to biological pre- and post-synaptic processes. In this configuration, the optical pulse serves as the pre-synaptic spike, providing a stimulus that generates photocarriers in the IGZO channel. The resulting transient drain current corresponds to the post-synaptic current (EPSC), representing the strength of the synaptic response. As the amplitude and duration of the optical pulse (spike voltage equivalent) increase, more photocarriers are excited and trapped, leading to a higher EPSC amplitude and prolonged decay. This relationship between the optical input and EPSC mirrors the coupling between pre-synaptic spike potential and post-synaptic response observed in biological synapses. The second pulse produces a higher peak current than the first, showing classic PPF behavior. The PPF retention was calculated using the first (A_1) and second (A_2) EPSC peaks, and, by the equation:

$$\mathrm{PPF}(\%) = \frac{A_2}{A_1} \times 100$$

Fig. 2d presents the PPF (%) results across 12 different conditions—six gate voltages under blue light and six under green light. In every case, PPF was observed. As the interval between pulses increased, retention decreased. This result reflects the recombination of photocarriers over time.[40–42] On the other hand, Fig. 2e shows the EPSC enhancement measured with increasing pulse lengths.[43–46] EPSC enhancement refers to the growth in EPSC area under repeated stimulation. It was calculated using the EPSC areas from single and repeated pulses, and, using the formula:

$$\mathrm{EPSC\,enhancement} = \frac{I_{\mathrm{peak}}}{I_{\mathrm{initial}}}$$

The data show that in all 12 conditions, EPSC increased steadily with longer pulse duration. This confirms that the device supports cumulative plasticity.[43] Even under strong negative gate voltages like −18 V, the EPSC enhancement remained reliable. This suggests the device maintains high sensitivity and stable response. The raw EPSC measurements used in these calculations are shown in Fig. S1 and S2. We further explored gate-tunable learning behavior using repeated training and relearning tests. Fig. 2f and g show EPSC changes during a cycle of 50 light pulses (learning), followed by 50 seconds without stimulation (forgetting), and 10 more pulses (relearning). Blue (405 nm) and green (520 nm) light were used, respectively. In both cases, EPSC showed a clear cycle of increase, decrease, and increase again. This reflects long-term synaptic plasticity like that seen in the brain.[46,47] Gate voltage clearly affected the EPSC: it was highest at −3 V and lowest at −18 V. This pattern was consistent under both wavelengths. It supports the idea that gate voltage works like a neuromodulator by setting synaptic sensitivity before the light input. Fig. S3 gives a closer view of the early response under different gate voltages. It shows that the timing and slope of EPSC growth shift with gate control. These observations demonstrate that our device can mimic short-term and long-term synaptic behaviors, such as facilitation, memory retention, and relearning. In addition, it offers adjustable gain control through gate voltage, enabling flexible light-driven synaptic response that can be fine-tuned ahead of stimulation that similar to biological neuromodulation.[30,38,43] Furthermore, Fig. S6 shows that the device maintains stable EPSC generation even under periodic blue light pulses delivered at a short 25 ms interval, confirming that the channel responds reliably to high-frequency optical stimulation without signal degradation. Fig. S7 further demonstrates that the EPSC magnitude varies systematically with input light intensity under both blue (450 nm) and green (520 nm) illumination. Higher optical intensity produced larger EPSC increments, indicating that the synaptic strength is jointly determined by gate-controlled carrier density and the density of photogenerated carriers. These results indicate that the interplay between gate-induced carrier depletion and light-generated photocarriers governs the EPSC magnitude, suggesting that carrier dynamics rather than optical intensity alone dictate synaptic strength.

Fig. 3 presents a comprehensive spectroscopic analysis of the IGZO layer, which clarifies the material's composition, defect states, and electronic structure that influence its photoresponsive behavior. Fig. 3a–d show the XPS spectra of the four main elements: In, Ga, Zn, and O. The In 3d peaks are centered around 445 eV and 453 eV (Fig. 3a), Ga 2p peaks appear near 1119 eV and 1145 eV (Fig. 3b), and Zn 2p peaks are located at approximately 1023 eV and 1046 eV (Fig. 3c). These data confirm that the IGZO layer includes all the intended elements, with an atomic ratio of In : Ga : Zn approximately 6.1 : 1 : 2.[48] The O 1s core-level spectrum (Fig. 3d) provides insights into the chemical environment of oxygen in the film.[49] It contains three distinct peaks at 530.0 eV, 531.5 eV, and 533.1 eV, which are attributed to lattice oxygen (M–O), oxygen vacancies, and hydroxyl groups (O–OH), respectively. The presence of a oxygen vacancy peak at 531.5 eV indicates defect states within the IGZO.[31] These vacancies are widely reported to introduce localized trap states inside the bandgap, which can play a critical role in modulating electrical conductivity and enabling light-induced persistent photoconductivity (PPC).[50,51] In particular, trapped carriers can be slowly released after photoexcitation, exhibit a sustained synaptic response resembling biological short-term memory.[52,53] The optical absorption properties of IGZO were evaluated using UV-vis spectroscopy. As shown in Fig. 3e, the Tauc plot yields an optical

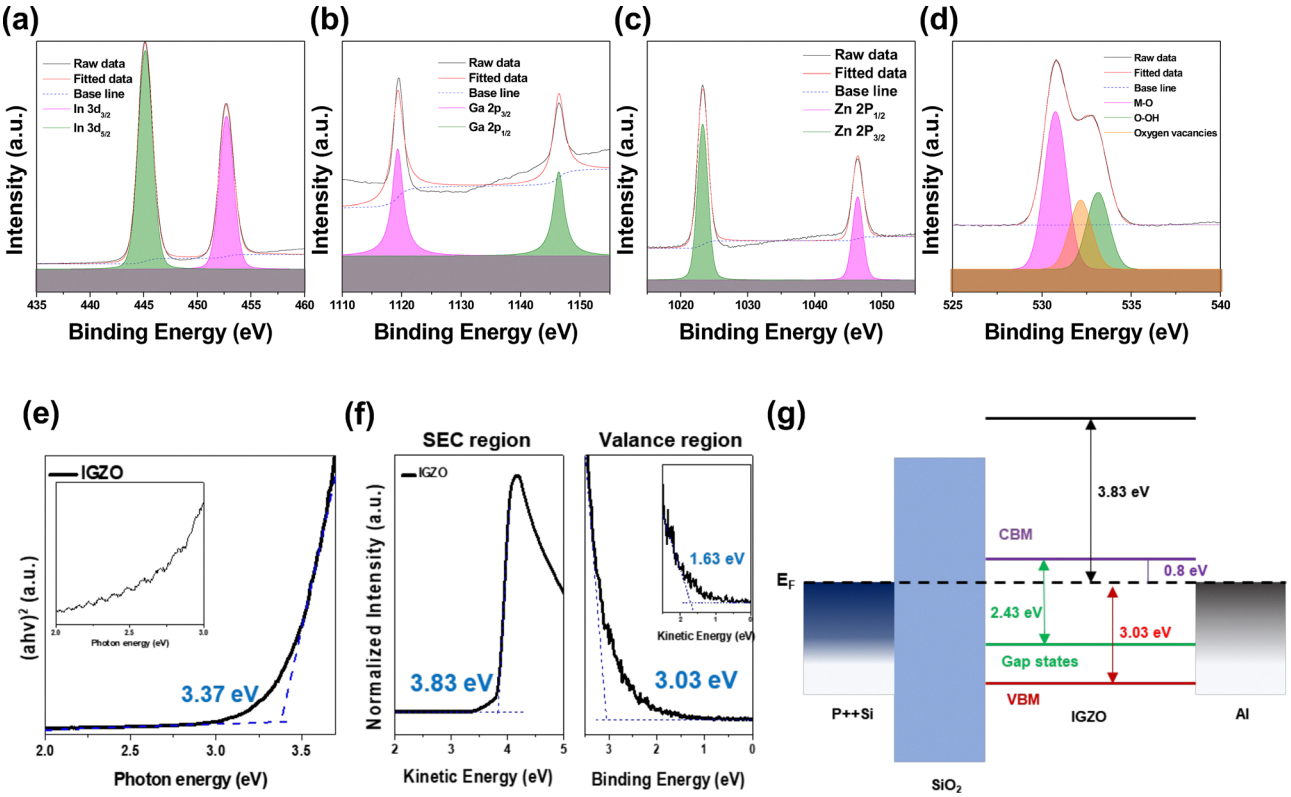

Fig. 3 (a–d) X-ray photoelectron spectroscopy (XPS) spectra confirming the presence of constituent elements in the IGZO film: (a) In 3d peaks (b) Ga 2p peaks (c) Zn 2p peaks (d) O 1s peaks, respectively. (e) UV-visible absorption spectrum of the IGZO film with Tauc plot (f) ultraviolet photoelectron spectroscopy (UPS) results of the IGZO film (g) energy band diagram constructed using the UV-vis and UPS data.

bandgap of approximately 3.37 eV. Notably, absorption starts to increase gradually below this value, suggesting the influence of sub-gap states. This deviation from ideal band-to-band absorption further supports the existence of oxygen-vacancy-induced states that extend the spectral response into the visible region.[54] Fig. 3f presents the ultraviolet photoelectron spectroscopy (UPS) results. The secondary electron cutoff gives a work function of 3.83 eV, and the valence band maximum (VBM) is located 3.03 eV below the Fermi level.[55] The inset image shows additional states detected at approximately 1.63 eV below the conduction band minimum (CBM), corresponding to oxygen-vacancy-related gap states.[56] These states are critical in enabling sub-bandgap optical transitions.[57] Based on the energy difference between the gap states and the CBM (~2.43 eV), the device can absorb green light (~520 nm, ~2.38 eV) *via* defect-assisted transitions. In addition, blue light (~450 nm, ~2.76 eV) has sufficient photon energy to excite electrons directly across the bandgap, further contributing to the device's optical response.[58] Fig. 3g schematically summarizes the band structure of IGZO constructed from the UPS and UV-vis data. The diagram illustrates the positions of the VBM, CBM, and mid-gap states associated with oxygen vacancies, clarifying the optical excitation pathways under different photon energies. Specifically, defect-assisted transitions enable sub-bandgap absorption of green light, whereas blue light excitation occurs *via* direct band-to-band transitions. This schematic highlights how oxygen-vacancy-related states expand the effective absorption window of IGZO into the visible region and provide a physical basis for the device's broadband photoresponsive and synaptic behavior. This demonstrates that oxygen vacancy–induced trap states extend the absorption window of IGZO into the visible region, enhancing its suitability for low-energy, broadband optical neuromorphic applications. The correlation between sub-gap optical absorption and oxygen-vacancy-related states confirms that intrinsic defect engineering is a viable route for tailoring optical synaptic gain in oxide semiconductors.

Fig. 4 explains the mechanism behind the gate-controlled synaptic behavior in the IGZO-based optical synaptic transistor. Fig. 4a–c show the band diagrams of the IGZO/SiO_2 interface under different gate voltages, and Fig. 4d–f present the corresponding cross-sectional schematics indicating the depletion region. At V_G = 0 (Fig. 4a and d), the CBM and VBM in the IGZO layer are nearly flat near the IGZO/SiO_2 interface, indicating the absence of significant band bending. The schematic confirms that the depletion region is negligible, allowing easy carrier transport when light is applied. Under these conditions, photogenerated carriers move freely, resulting in the largest EPSC among the three cases. When a moderate negative gate voltage of –3 V is applied (Fig. 4b and e), a slight upward band bending occurs at the IGZO/SiO_2 interface, producing a shallow depletion region that partially extends into the IGZO/SiO_2 interface. This depletion region moderately restricts carrier movement, so photogenerated electrons are more difficult to

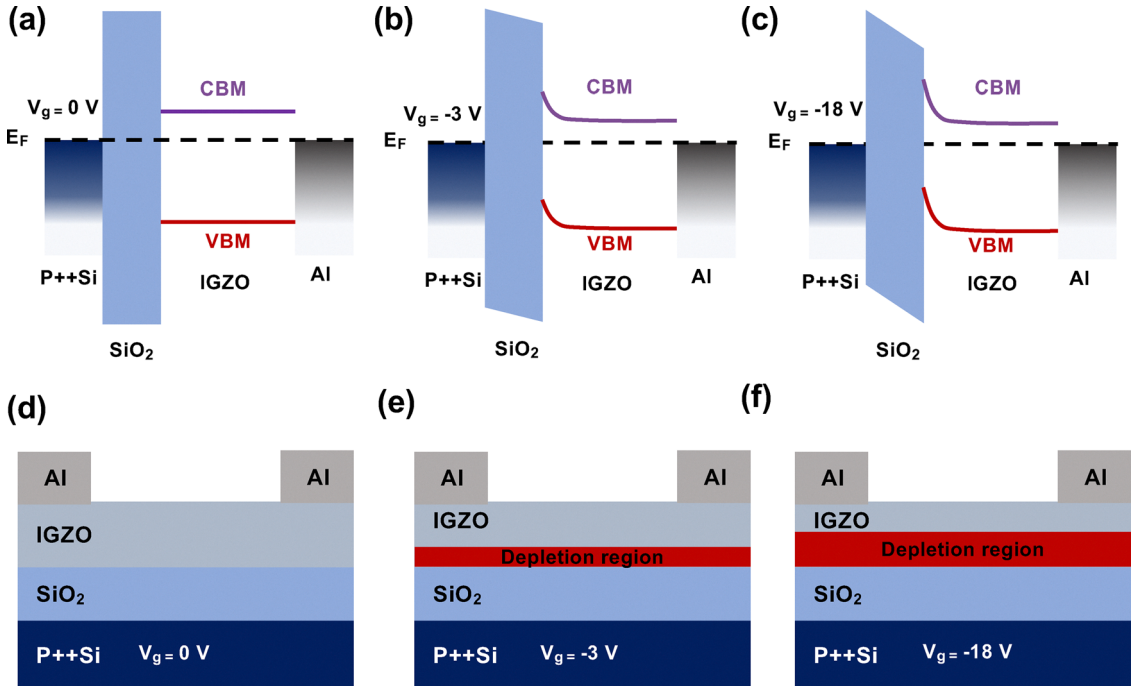

Fig. 4 Gate-voltage-dependent band diagrams (a–c) and cross-sectional schematics (d–f) of the IGZO-based optical synaptic transistor, showing the depletion region at the IGZO/SiO_2 interface under V_G = 0 V (a and d), −3 V (b and e), and −18 V (c and f).

transport than at 0 V.[59–62] As a result, the EPSC amplitude decreases compared to 0 V, but remains considerable. At a stronger negative gate voltage of −18 V (Fig. 4c and f), the band bending becomes much more severe. The depletion region significantly expands. This large depletion width severely limits the photogenerated carrier movement, strongly suppressing the photocurrent under identical optical input. As a result, the EPSC amplitude becomes very small, even under the same optical stimulation. This gradual expansion of the depletion region explains the changes in EPSC seen earlier in Fig. 2f and g. In this way, the gate voltage can be used ahead of light input to adjust the sensitivity of the device. This analysis clarifies that gate-induced band bending serves as an external control parameter for neuromodulatory gain regulation, providing a direct physical mechanism for adaptive learning behavior.

Fig. 5 evaluates how the gate-tunable synaptic behavior of the proposed IGZO optical transistor affects high-level machine vision tasks using the CIFAR-10 dataset and a CNN model. In Fig. 5a, a schematic illustrates the integration of the device into a learning system. Identical visual input images from CIFAR-10 are processed, and the device's EPSC levels, which vary depending on the gate voltage, are used to set the synaptic weights delivered to the CNN model. The normalized EPSC values for each gate condition were directly applied as scaling factors to the synaptic connections in both the convolutional and dense layers, allowing the gate-dependent device behavior to influence feature extraction and classification processes simultaneously. This connection ensures that the physical characteristics of the device contribute to the learning efficiency throughout the network rather than only during initialization. Here, the CNN is not intended to replicate full hardware-in-the-loop learning. Instead, it serves as a functional-level validation tool to examine how gate-controlled EPSC modulation biases the learning trajectory under identical network architectures and training conditions.

For statistical evaluation, five independent CNN models were trained for each condition using different random seeds, and the resulting accuracies were analyzed in terms of their mean values and standard deviations, as summarized in Fig. S8. The results shown in Fig. S8 indicate that the overall performance trends are preserved despite variations in random initialization. In particular, the device-modulated CNNs under the same gate bias exhibit comparable accuracy distributions across repeated trials, while the baseline CNN trained with standard random weight initialization serves as a consistent reference across the same set of random seeds. Importantly, the relative performance relationships between the baseline model and the device-modulated conditions at −3 V and −18 V remain unchanged across independent runs. These observations confirm that the reported CNN performance reflects a reproducible and statistically consistent trend rather than being strongly influenced by a specific random initialization, thereby supporting the validity of the device-derived weight modulation scheme.

In this study, the device was not used to directly capture visual images. Instead, experimentally measured EPSC values obtained under different gate voltages and illumination conditions were normalized and used as synaptic weight-scaling factors in the CNN model. These normalized weights were then applied to the CIFAR-10 dataset during training and testing, enabling simulation of how the device's gate-dependent synaptic

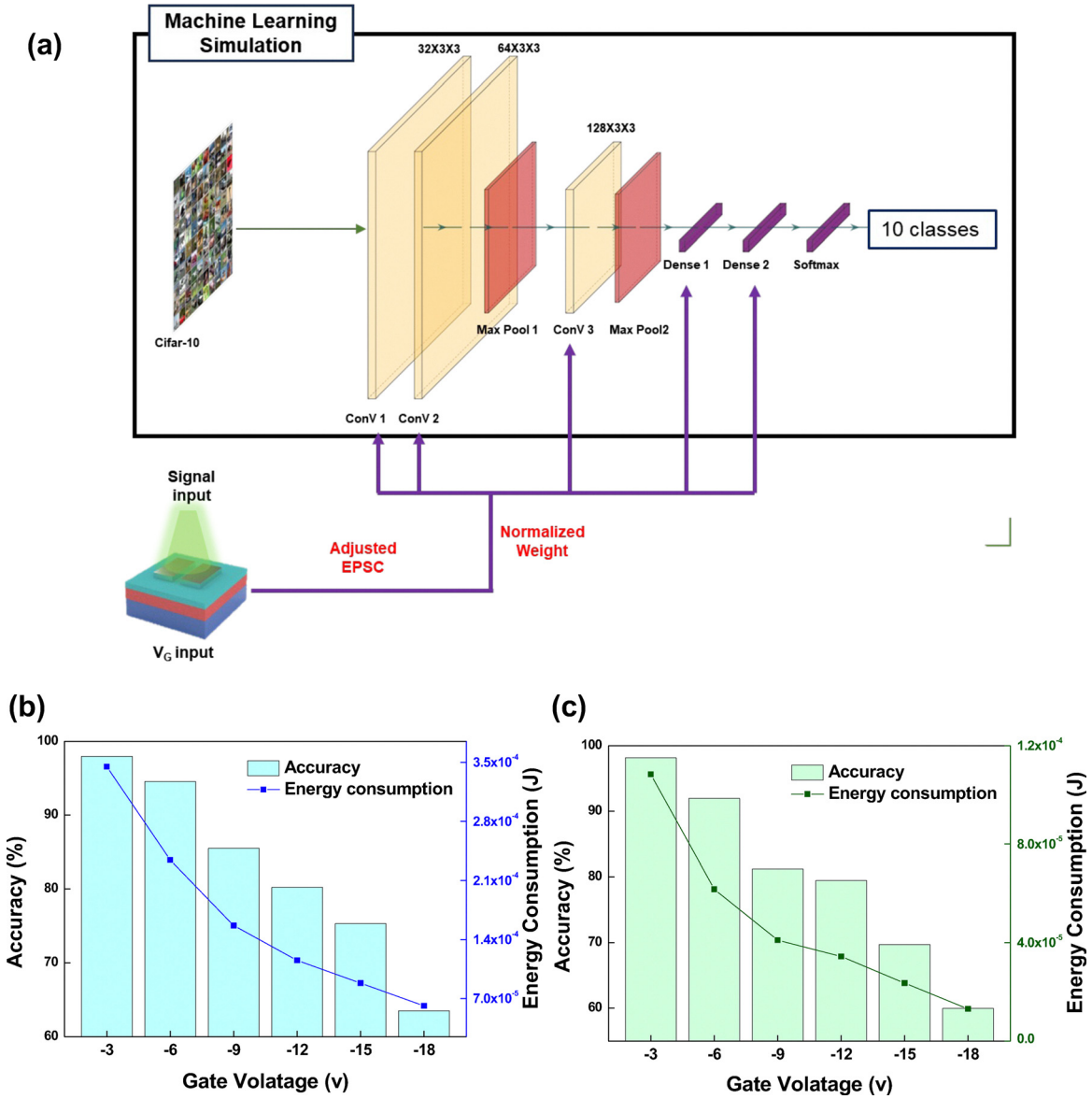

Fig. 5 (a) Schematic illustration of the CIFAR-10 image classification process using a CNN model trained with synaptic weights derived from the gate-tunable EPSC values of the IGZO-based optical synaptic transistor. (b and c) Classification accuracy (left y-axis) and estimated energy consumption per pulse (right y-axis) under 450 nm blue (b) and 520 nm green (c) illumination, as a function of gate voltage.

behavior influences learning performance. Therefore, the CNN training and inference were performed through a hardware-inspired simulation using experimentally derived device characteristics rather than direct hardware image sensing. This approach allows evaluation of how gate-dependent synaptic modulation influences learning accuracy and energy consumption in a neuromorphic vision system.[10] The CNN model includes three convolutional layers (32, 64, and 128 filters), with max pooling applied after the second and third layers. These layers are followed by two dense layers and a final softmax output layer for classification. Higher EPSC values, induced by less negative gate voltages, result in larger weight values being passed to the CNN, while lower EPSC values lead to smaller weights. Fig. 5b and c show the resulting test accuracies and energy consumption values after 20 training epochs under blue (450 nm) and green (520 nm) light, respectively. In both figures, higher gate voltages lead to greater EPSC enhancement, as shown in Fig. 2, resulting in a clear improvement in CNN classification accuracy. Under blue light (405 nm), the test accuracy was about 96% at $V_G = -3$ V and 60% at $V_G = -18$ V, while under green light (520 nm), it was about 94% at $V_G = -3$ V and 57% at $V_G = -18$ V.[38] However, this improvement in classification performance comes at the cost of increased energy consumption. We note that randomly initialized networks may eventually reach comparable accuracy given sufficient training. However, the purpose of this study is not to maximize final accuracy, but to demonstrate that gate-tunable EPSC presets learning sensitivity and enables controllable accuracy–energy tradeoffs under constrained training budgets.

The energy consumption for each optical stimulus was estimated using the following equation:[28,29]

$$E_c = I_{peak} \times V_{DS} \times t_{pulse}$$

where E_c is the energy consumed per pulse, I_{peak} is the peak EPSC value after illumination, V_{DS} is the drain-source voltage, and t_{pulse} is the duration of the optical pulse. At higher gate voltages, the increased carrier concentration in the IGZO layer during illumination leads to higher current values I_{peak}, which directly increases energy usage. Conversely, at lower gate voltages such as −18 V, the current level is suppressed due to strong band bending and carrier depletion (as discussed in Fig. 4), which leads to much lower energy consumption but also reduces the final accuracy of the CNN model. This tradeoff between energy and accuracy resembles a core feature of biological synapses, where the strength of a connection can be regulated depending on the situation.[62] In the human brain, strong neurotransmitter signals or neuromodulator activity can improve learning performance, though this requires more metabolic energy.[63] Likewise, our device allows the synaptic output strength (EPSC) to be adjusted in advance through gate voltage, enabling different modes of learning.[64] For example, using a high gate voltage setting can be helpful when high recognition accuracy is needed.[65] On the other hand, when power saving is more important, a lower gate voltage can be applied to reduce energy consumption while still keeping a usable level of accuracy. These results show that the IGZO device not only adjusts synaptic strength but also offers a straightforward way to control energy-accuracy balances, making it a suitable platform for neuromorphic vision systems that need to respond to changing conditions. Therefore, the CNN performance variations observed here originate from physically measured EPSC differences, demonstrating that material-level modulation can be functionally translated into network-level learning efficiency.

4. Conclusion

In this work, we demonstrated an IGZO-based optical synaptic transistor whose synaptic response can be modulated by the gate voltage. Material and electrical characterizations confirmed that oxygen vacancies in the IGZO channel create trap states, enabling the device to absorb visible light. These trap states facilitate photoexcited carrier generation even at lower photon energies, broadening the device's optical response range. The device successfully emulated key synaptic behaviors such as PPF, EPSC enhancement, and re-learning. More importantly, the strength of these responses could be tuned *via* gate voltage, similar to biological neuromodulation. This external control allowed the device to exhibit different memory and learning levels from identical optical input. The measured EPSC characteristics were applied to a CNN model for CIFAR-10 image classification, showing that higher gate voltages improved accuracy but increased energy consumption. This trade-off illustrates how the device can be flexibly operated depending on system power or accuracy requirements. Overall, the proposed IGZO synaptic transistor combines a simple structure, broad visible-light sensitivity, controllable synaptic behavior, and power-adaptive learning capability, making it a promising platform for practical, low-power, and adaptive neuromorphic vision systems.

Author contributions

J. M. Y and S. J. K planned the experiment. J. M. Y and Y. B. K fabricated the IGZO synaptic transistors and conducted the experimental analysis. J. M. Y, Y. B. K and M. J. C examine the data obtained from measurements. J. M. Y drafted the manuscript, and it was confirmed and edited by S. J. K. S. J. K supervised the project. All authors have approved the final version of the manuscript.

Conflicts of interest

There are no conflicts to declare.

Data availability

The authors declare that all data supporting the findings of this study are available within the paper and its supplementary information (SI). Supplementary information is available. See DOI: https://doi.org/10.1039/d5mh02224j.

Acknowledgements

This research was supported by Basic Science Research Program through the National Research Foundation of Korea (NRF) funded by the Ministry of Education (RS-2020-NR049601 and RS-2025-00523190).

References

1 H. Xu, L. Zou, J. An and S. Lin, *ACS Omega*, 2025, **10**, 16884–16891.
2 Y. Kim, C. W. Lee and H. W. Jang, *J. Electron. Mater.*, 2025, **54**, 3609–3650.
3 J. Zhu, T. Zhang, Y. Yang and R. Huang, *Appl. Phys. Rev.*, 2020, **7**, 011312.
4 S. W. Cho, S. M. Kwon, Y.-H. Kim and S. K. Park, *Adv. Intell. Syst.*, 2021, **3**, 2000162.
5 S. Dai, Y. Zhao, Y. Wang, J. Zhang, L. Fang, S. Jin, Y. Shao and J. Huang, *Adv. Funct. Mater.*, 2019, **29**, 1903700.
6 Y. Wang, L. Yin, W. Huang, Y. Li, S. Huang, Y. Zhu, D. Yang and X. Pi, *Adv. Intell. Syst.*, 2021, **3**, 2000099.
7 J. H. Jeong, J. H. Ma, M. H. Park, H. J. Ha, S. J. Kang, J. M. Yun, Y. B. Kim, E. Kim and S. J. Kang, *Adv. Funct. Mater.*, 2024, **34**, 2402222.
8 H. Wei, Y. Ni, L. Sun, H. Yu, J. Gong, Y. Du, M. Ma, H. Han and W. Xu, *Nano Energy*, 2021, **81**, 105648.
9 H. Wang, J. Hu, Y. Baek, K. Tsuchiyama, M. Joly, Q. Liu and S. Gigan, *Light: Sci. Appl.*, 2025, **14**, 245.
10 Z. Hou, J. Shen, Y. Zhong and D. Wu, *Micromachines*, 2025, **16**, 517.

11 M. H. Park, Y. Kim, M. J. Choi, Y. B. Kim, J. M. Yun, J. H. Jeong, S. Kim, S. Park and S. J. Kang, *ACS Nano*, 2025, **19**, 13107–13117.
12 Y. Chai, J. Kim, H. J. Kim and J. S. Park, *ACS Appl. Electron. Mater.*, 2020, **2**, 310–317.
13 Y. Yang, C. Pan, Y. Li, X. Yangdong, P. Wang, Z.-A. Li, S. Wang, W. Yu, G. Liu and B. Cheng, *Nat. Electron.*, 2024, **7**, 225–233.
14 J. Yu, Y. Wang, S. Qin, G. Gao, C. Xu, Z. L. Wang and Q. Sun, *Mater. Today*, 2022, **60**, 158–182.
15 S. Dai, X. Liu, Y. Liu, Y. Xu, J. Zhang, Y. Wu, P. Cheng, L. Xiong and J. Huang, *Adv. Mater.*, 2023, **35**, 2300329.
16 S. Zhang, J. Zhu, R. Qiu, D. Liu, Q. Ren and M. Zhang, *Adv. Mater.*, 2025, 2418418.
17 S. Shrivastava, H. Juliano, P. A. L. Uong and T.-Y. Tseng, *APL Electron. Dev.*, 2025, **1**, 021506.
18 T. Sun, B. Feng, J. Huo, Y. Xiao, W. Wang, J. Peng, Z. Li, C. Du, W. Wang and G. Zou, *Nano-Micro Lett.*, 2024, **16**, 14.
19 L. K. Krugel, G. Biele, P. N. Mohr, S.-C. Li and H. R. Heekeren, *Proc. Natl. Acad. Sci. U. S. A.*, 2009, **106**, 17951–17956.
20 L. Speranza, U. Di Porzio, D. Viggiano, A. de Donato and F. Volpicelli, *Cells*, 2021, **10**, 735.
21 P. Salvan, M. Fonseca, A. M. Winkler, A. Beauchamp, J. P. Lerch and H. Johansen-Berg, *Nat. Neurosci.*, 2023, **26**, 53–63.
22 S. Jiang, X. Wu, N. J. Rommelfanger, Z. Ou and G. Hong, *Natl. Sci. Rev.*, 2022, **9**, nwac007.
23 O. Karatum, M.-J. Gwak, J. Hyun, A. Onal, G. R. Koirala, T.-I. Kim and S. Nizamoglu, *Chem. Soc. Rev.*, 2023, **52**, 3326–3352.
24 C. Yang, Z. Cheng, P. Li and B. Tian, *Acc. Chem. Res.*, 2024, **57**, 1398–1410.
25 Z. Yin, L. Shan, R. Ci, D. Hao, G. Miao, L. Tian, G. Liu and F. Shan, *Appl. Phys. Lett.*, 2025, **126**, 103302.
26 X. Liu, D. Li, Y. Wang, D. Yang and X. Pi, *APL Mach. Learn.*, 2023, **1**, 031501.
27 H.-S. Kim, H. Park and W.-J. Cho, *Biomimetics*, 2023, **8**, 532.
28 H. Xie, G. Miao, G. Liu and F. Shan, *Appl. Phys. Lett.*, 2024, **124**, 233301.
29 J. Jang, S. Park, D. Kim and S. Kim, *Sens. Actuators, A*, 2024, **376**, 115641.
30 L. Hu, X. Zhuge, J. Wang, X. Wei, L. Zhang, Y. Chai, X. Xue, Z. Ye and F. Zhuge, *Adv. Electron. Mater.*, 2025, **11**, 2400482.
31 J. H. Ma, J. H. Jeong, S. J. Kang, M. H. Park, H. J. Ha, E. Kim, S. You, W. Kim, S. Park and S. J. Kang, *Adv. Opt. Mater.*, 2024, **12**, 2400166.
32 M. Abadi, P. Barham, J. Chen, Z. Chen, A. Davis, J. Dean, M. Devin, S. Ghemawat, G. Irving and M. Isard, Proceedings of the 12th USENIX Symposium on Operating Systems Design and Implementation (OSDI 16), 2016, 265–283.
33 X. Glorot and Y. Bengio, *JMLR Workshop and Conference Proceedings*, 2010, 249–256.
34 F. Chollet, *Astrophysics source code library*, 2018, ascl: 1806.1022.
35 C. Zhu, H. Liu, W. Wang, L. Xiang, J. Jiang, Q. Shuai, X. Yang, T. Zhang, B. Zheng and H. Wang, *Light: Sci. Appl.*, 2022, **11**, 337.
36 Y. Jang, J. Park, J. Kang and S.-Y. Lee, *ACS Appl. Electron. Mater.*, 2022, **4**, 1427–1448.
37 J. Sun, S. Oh, Y. Choi, S. Seo, M. J. Oh, M. Lee, W. B. Lee, P. J. Yoo, J. H. Cho and J. H. Park, *Adv. Funct. Mater.*, 2018, **28**, 1804397.
38 L. Q. Guo, L. Q. Zhu, J. N. Ding and Y. K. Huang, *AIP Adv.*, 2015, **5**, 057121.
39 S. Park, S. Kim, S. Kim, K. Park, D. Ryu and S. Kim, *Adv. Opt. Mater.*, 2025, 2500634.
40 Y. Wang, G. Miao, Z. Yin, R. Ci, G. Liu and F. Shan, *Appl. Phys. Lett.*, 2025, **127**, 013501.
41 C. Fu, Z.-Y. Li, Y.-J. Li, M.-M. Zhu, L.-B. Luo, S.-S. Jiang, Y. Wang, W.-H. Wang and G. He, *J. Mater. Sci. Technol.*, 2024, **196**, 190–199.
42 H. Komatsu, T. Ogawa, N. Hosoda and T. Ikuno, *AIP Adv.*, 2024, **14**, 035062.
43 S. Lan, J. Zhong, J. Chen, W. He, L. He, R. Yu, G. Chen and H. Chen, *J. Mater. Chem. C*, 2021, **9**, 3412–3420.
44 J. Zhang, S. Dai, Y. Zhao, J. Zhang and J. Huang, *Adv. Intell. Syst.*, 2020, **2**, 1900136.
45 C. Gonzalez-Islas and J. J. Hablitz, *J. Neurosci.*, 2003, **23**, 867–875.
46 X. Jin, D. A. Prince and J. R. Huguenard, *J. Neurosci.*, 2006, **26**, 4891–4900.
47 J.-H. Oh, J.-H. Kim, H.-J. Kim, Y. H. Kim, K.-K. Kim and S.-N. Lee, *Adv. Intell. Syst.*, 2023, **5**, 2300350.
48 Y. Han, J. Seo, D. H. Lee and H. Yoo, *Micromachines*, 2025, **16**, 118.
49 Q. Shangguan, Y. Lv and C. Jiang, *Nanomaterials*, 2024, **14**, 1679.
50 X. Zhou, J. Xu, L. Yang, X. Tang, Q. Wei and Z. Yu, *Opt. Mater. Express*, 2015, **5**, 1628–1634.
51 A. de Jamblinne de Meux, A. Bhoolokam, G. Pourtois, J. Genoe and P. Heremans, *Phys. Status Solidi A*, 2017, **214**, 1600889.
52 Y. Kang, H. Song, H.-H. Nahm, S. H. Jeon, Y. Cho and S. Han, *APL Mater.*, 2014, **2**, 092512.
53 M. E. Pereira, J. Deuermeier, R. Martins, P. Barquinha and A. Kiazadeh, *ACS Appl. Electron. Mater.*, 2024, **6**, 5230–5243.
54 R. N. Vemuri, W. P. Mathews, M. Marrs and T. Alford, *J. Phys. D: Appl. Phys.*, 2012, **46**, 045101.
55 Q.-J. Sun, J. Wu, M. Zhang, Y. Yuan, X. Gao, S.-D. Wang, Z. Tang, C.-C. Kuo and Y. Yan, *Phys. Status Solidi A*, 2022, **219**, 2200311.
56 K. T. Vogt, C. E. Malmberg, J. C. Buchanan, G. W. Mattson, G. M. Brandt, D. B. Fast, P. H.-Y. Cheong, J. F. Wager and M. W. Graham, *Phys. Rev. Res.*, 2020, **2**, 033358.
57 L. Meng, H. Hao, L. Ma, H. Yue, H. Ye, L. Guo, Z. Huang and L. Tian, *Appl. Surf. Sci.*, 2025, **701**, 163266.
58 A. Sen, H. Park, P. Pujar, A. Bala, H. Cho, N. Liu, S. Gandla and S. Kim, *ACS Nano*, 2022, **16**, 9267–9277.
59 M. Mativenga, F. Haque, M. M. Billah and J. G. Um, *Sci. Rep.*, 2021, **11**, 14618.
60 J. Oh, K. M. Jung, J. Lee, E. K. Jung, J. H. Jeon, K. Park and Y. S. Kim, *J. Soc. Inf. Disp.*, 2019, **27**, 776–784.
61 A. Barua, K. D. Leedy and R. Jha, *Solid State Electron. Lett.*, 2020, **2**, 59–66.

62 L. F. Herbozo Contreras, N. D. Truong, J. K. Eshraghian, Z. Xu, Z. Huang, T. V. Bersani–Veroni, I. Aguilar, W. H. Leung, A. Nikpour and O. Kavehei, *PNAS nexus*, 2024, **3**, pgae488.
63 S. Luan, I. Williams, K. Nikolic and T. G. Constandinou, *Front. Neuroeng.*, 2014, **7**, 27.
64 H. L. Li and M. C. Van Rossum, *eLife*, 2020, **9**, e50804.
65 C. Weilenmann, A. N. Ziogas, T. Zellweger, K. Portner, M. Mladenović, M. Kaniselvan, T. Moraitis, M. Luisier and A. Emboras, *Nat. Commun.*, 2024, **15**, 6898.